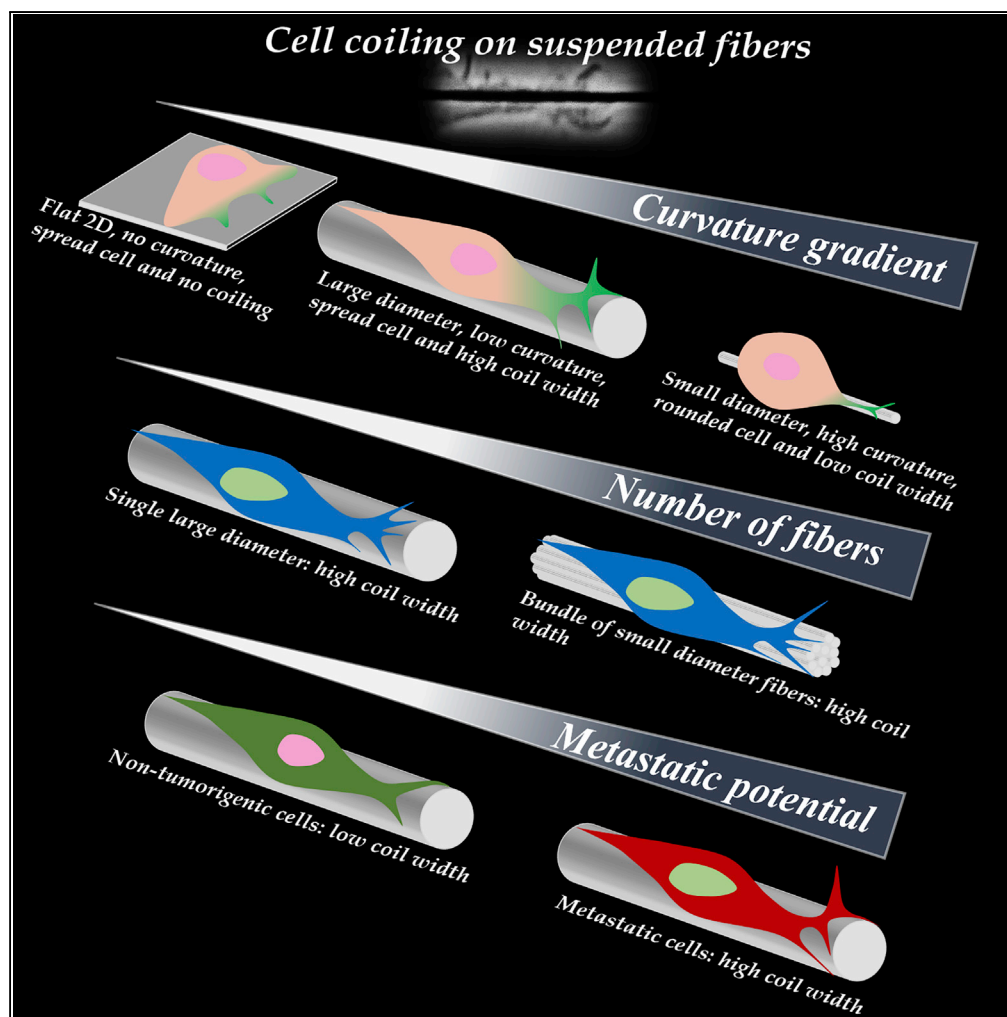


Article

Cancer Cells Sense Fibers by Coiling on them in a Curvature-Dependent Manner



Apratim Mukherjee,
Bahareh Behkam,
Amrinder S. Nain

nain@vt.edu

HIGHLIGHTS

Cells sense ECM-mimicking suspended fibers by coiling (wrapping around)

Coiling occurs at the tip of growing protrusions in a curvature-dependent manner

Non-tumorigenic cells exhibit diminished coiling compared with metastatic cells

A bundle of small-diameter fibers recover coiling observed on a large-diameter fiber

Mukherjee et al., iScience 19, 905–915
September 27, 2019 © 2019
The Author(s).
<https://doi.org/10.1016/j.isci.2019.08.023>

Article

Cancer Cells Sense Fibers by *Coiling* on them in a Curvature-Dependent Manner

Apratim Mukherjee,¹ Bahareh Behkam,¹ and Amrinder S. Nain^{1,2,*}**SUMMARY**

Metastatic cancer cells sense the complex and heterogeneous fibrous extracellular matrix (ECM) by formation of protrusions, and our knowledge of how cells physically recognize these fibers remains in its infancy. Here, using suspended ECM-mimicking isodiameter fibers ranging from 135 to 1,000 nm, we show that metastatic breast cancer cells sense fiber diameters differentially by *coiling* (wrapping-around) on them in a curvature-dependent manner, whereas non-tumorigenic cells exhibit diminished *coiling*. We report that *coiling* occurs at the tip of growing protrusions and the *coil width* and *coiling rate* increase in a curvature-dependent manner, but time to maximum *coil width* occurs bi-physically. Interestingly, bundles of 135-nm diameter fibers recover *coiling width* and *rate* on 1,000-nm-diameter fibers. *Coiling* also coincides with curvature-dependent persistent and ballistic transport of endogenous granules inside the protrusions. Altogether, our results lay the groundwork to link biophysical sensing with biological signaling to quantitate pro- and anti-invasive fibrous environments.

INTRODUCTION

Protrusions are extensions from the cell body that are diverse in shape, molecular structure, and location relative to the cell body and play an important role in cell migration and extracellular matrix (ECM) degradation (Blanchoin et al., 2014; Clainche and Carlier, 2008; Koons et al., 2017; Machacek et al., 2009; Pollard and Borisy, 2003). The importance of protrusions as the precursor to migration (Alblazi and Siar, 2015; Friedl and Wolf, 2010; Ponti et al., 2004), in the presence of biophysical (Harland et al., 2011; Lo et al., 2000) and biochemical cues (Rhoads and Guan, 2007; Weber et al., 2013; Wu et al., 2012; Zigmond et al., 2001), is widely documented. In the context of cancer, specialized protrusive structures are known to break down the surrounding extracellular milieu (Buccione et al., 2004; Linder, 2007; Weaver, 2006).

The ECM through which cells navigate is a complex fibrous network that is composed of a wide range of fiber diameters (tens of nanometers to micrometers; Clark et al., 1982; Ushiki, 2002). *In vitro* assays, by us and others, have shown that the fiber diameter can have a significant impact on cell behavior by inducing changes in the morphology and redistribution of focal adhesion arrangements (Kennedy et al., 2017; Meehan and Nain, 2014). Using 3D gel assays, recent studies have reported that protrusions can remodel collagen fibers in the matrix in a “hand-over-hand” cycle at the leading edge (Meshel et al., 2005; Starke et al., 2013) or lateral to cell body (Wolf and Friedl, 2009), and aligned fibers in the gel limit formation of lateral protrusions, thus promoting cell persistence (Fraleley et al., 2015; Riching et al., 2014). It has also been shown that cells seeded in 3D gels form multiple protrusions simultaneously to “probe” the surrounding matrix fibers before extending a single, stable protrusion to define a front-rear axis (Carey et al., 2016). Although these investigations have yielded valuable information on the nature of protrusions, our current understanding of how cells biophysically sense ECM fibers remains in infancy.

Using suspended network of fibers of contrasting curvatures (*protrusive* assay) that decouples bulk cell body migration from protrusive dynamics, we have previously shown that normal breast epithelial cells MCF 10A form shorter protrusions compared with the highly metastatic breast adenocarcinoma MDA-MB-231 on fibers of varying diameters (Koons et al., 2017). Briefly, our method allows us to constrain the cell body on large-diameter ($\geq 2 \mu\text{m}$) *base fibers*, whereas orthogonally deposited smaller diameter *protrusive fibers* elicit protrusive events. Using this platform, here, we report that migratory cells *coil* (wrap-around, [Video S1](#)) on fibers of varying curvature differentially. *Coiling* at the tip of protrusions occurs in bursts during growth phase of protrusions, which synchronizes with endogenous translocation of lipid granules inside protrusions along linear tracks in a persistent superdiffusive manner. Interestingly, depositing a bundle of densely packed small-diameter fibers recovers *coiling* dynamics of single large-diameter

¹Department of Mechanical Engineering, Virginia Tech, Blacksburg, VA 24061, USA

²Lead Contact

*Correspondence: nain@vt.edu

<https://doi.org/10.1016/j.isci.2019.08.023>



fibers. We also quantitate *coiling* by migrating cells in spindle shapes on single suspended fibers (*migration assay*). We report notable differences in *coiling* behavior between *protrusive* and *migration* assays on large-diameter fibers. For the breast cancer model used in this study, we report that non-tumorigenic MCF 10A exhibit diminished *coiling* in low numbers compared with their metastatic counterparts (MDA-MB-231 and BT-549). Altogether, our results using ECM-mimicking fibers lay the groundwork to link biophysical cell sensing with biological signaling to define pro- and anti-invasive fibrous environments.

RESULTS

We used the non-electrospinning Spinneret-based Tunable Engineered Parameters (STEP) platform (Nain et al., 2009; Wang and Nain, 2014) to quantitate protrusion *coiling* behavior and the dynamics of endogenous granule transport into the protrusions as a function of *protrusive* fiber diameter at high spatio-temporal resolutions (sub-micron and 1 s). To study individual protrusions perpendicular to cell body direction, we used mismatch of fiber diameters with the *base* fiber at least 2 μm in diameter while five different *protrusive* fiber isodiameters (Figure 1A) were selected to be 135 ± 3 nm ($n = 71$), 269 ± 3 nm ($n = 51$), 453 ± 4 nm ($n = 36$), 597 ± 8 nm ($n = 30$), and $1,013 \pm 19$ nm ($n = 40$) (Nain and Wang, 2013). We use two morphodynamic metrics, the protrusion length (L) and eccentricity (E), to quantitate protrusion formation, growth, and retraction to the main cell body (*protrusive cycle*) (Figures 1A and 1B). (Koons et al., 2017) From optical microscopic images, acquired at 63 \times and 1-s interval (Videos S2, S3, and S4 for 135, 600, and 1,000 nm diameter, respectively), we observed that the protrusion tip *coils* (wraps around the suspended fiber axis; Figure 1C) such that a *coiling cycle* is characterized by an increase in the width of the *coil* till a maximum width is reached followed by a subsequent decrease (Figures 1D and 1E).

Timing of Coiling Is Modulated by Fiber Curvature

To develop the framework to study the details of the *coiling* behavior on fibers of varying diameters, we defined additional metrics: maximum *coil width* occurring during one *coiling cycle* (Figure 1E), *coil growth rate*, and the time taken to reach maximum *coil width*. We observed that *coiling* occurred in “spurts” at the onset of protrusion growth (Figure 2A) where the protrusion growth phase is quantitatively represented by a concomitant increase in both protrusion length and eccentricity (Figure 2A (i, ii), more representative profiles are included in Figure S1). Next, we wanted to determine the relationship between protrusion eccentricity (broadening of protrusion base) and *coiling*. Given the dynamic, fluctuating nature of protrusions, we conducted a transient analysis of the evolution of eccentricity before and after *coiling* initiation (Figure 2B (i), with *coiling* initiation shown by $t = 0$). We observed that for the intermediate *protrusive* fiber categories (~ 270 – ~ 600 nm), growth in eccentricity occurred before the initiation of *coiling*. However, for the fiber diameters on either end of the spectrum (high curvature 135 nm and low curvature 1,000 nm), we observed that *coiling* started independent of the broadening in the protrusion base. During the *coiling* process, protrusions were found to elongate (elongation shown schematically in Figure 1E) in a biphasic diameter-dependent fashion (Figure 2B (ii)), and the protrusions continued to increase in length even after the termination of the *coiling* behavior. To quantify eccentricity-*coiling* relationship, we looked at the average eccentricity value at the initiation of *coiling* as a function of fiber diameter and found that for the intermediate-fiber-diameter category (~ 270 , ~ 450 , and ~ 600 nm), the average eccentricity at the onset of *coiling* was at least 0.76 ± 0.02 , whereas for the ~ 135 - and $\sim 1,000$ -nm cases it averaged 0.51 ± 0.04 and 0.47 ± 0.05 , respectively (Figure 2B (iii)). We quantitated the time taken to initiate *coiling* (total time taken from the initial increase in protrusion eccentricity to the initiation of *coiling*), and consistent with average eccentricity values, found that on the small- and large-diameter fibers it took less time to initiate *coiling* (Figure 2B (iv)). Interestingly, we did not observe significance in total length of protrusion at *coiling* initiation or the number of *coiling* events occurring in an hour (Figure S2). Overall, we found that the average eccentricity at *coiling* initiation and its timing exhibited a biphasic response with increase in diameter followed by drop at $\sim 1,000$ nm.

Individual Coiling Dynamics Are Fiber Curvature Dependent

Having quantitated the interplay between increase in protrusion length during *coiling*, eccentricity, and *coiling* initiation, we next wanted to analyze the kinetics of *coil* growth. Observing *coiling* profiles on different fiber diameters (representative profiles in Figure 3A), we found that the maximum width of the *coil*, the *rate* at which the *coil* grows, and the time taken to reach the maximum *coil width* are modulated by fiber diameter. For both maximum *coil width* and the growth *rate*, we observed no significant differences between the two smallest diameter categories (~ 135 and ~ 270 nm). However, with further increase in

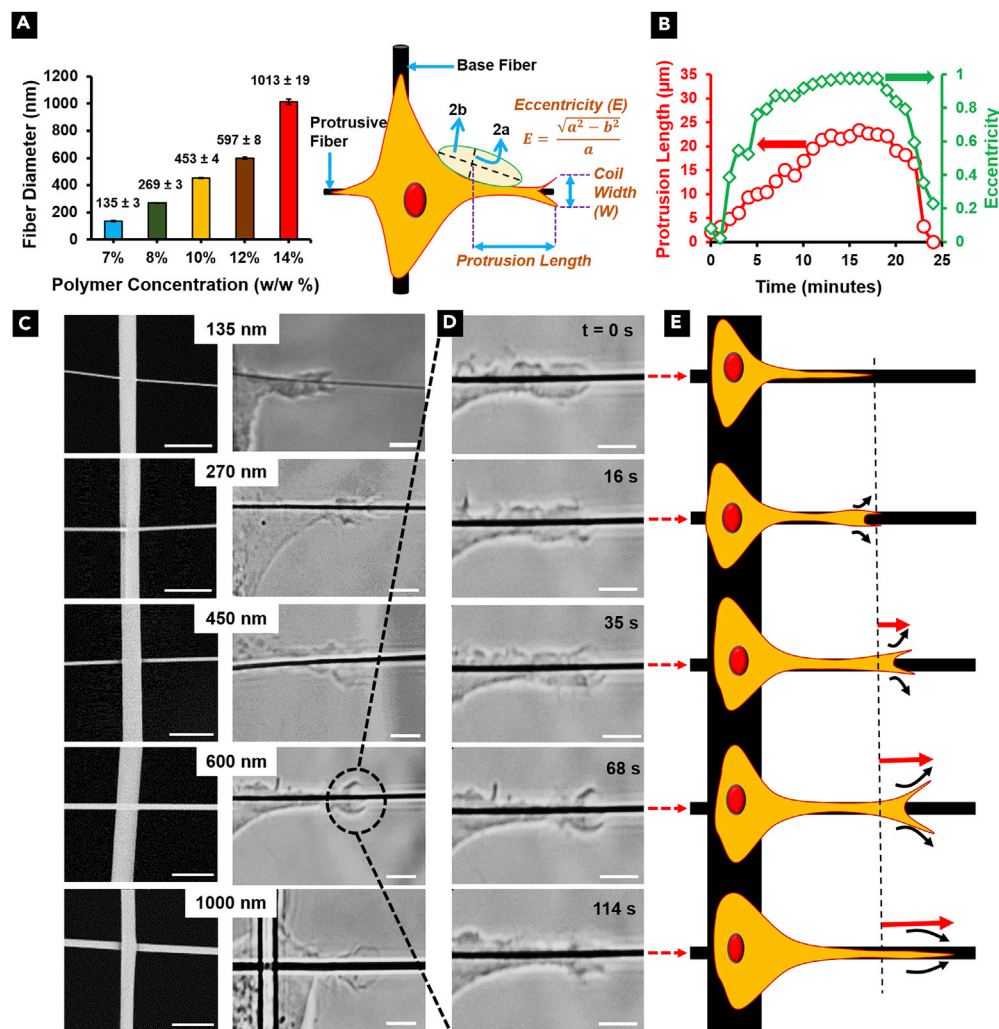


Figure 1. Morphodynamic Metrics used to Quantify Protrusive Behavior and Coiling Dynamics on Protrusive Assay

(A) Schematic showing the STEP protrusion platform (large-diameter *base* fibers deposited orthogonally onto smaller diameter *protrusive* fibers) along with metrics used to quantitate protrusive cycle and protrusion *coiling*. On left are data showing control on *protrusive* fiber diameter using STEP platform (n = 71, 51, 36, 30, and 40 for 135, 270, 450, 600, and 1,000 nm, respectively).

(B) Representative transient *protrusive* cycle showing protrusion growth and retraction to cell body.

(C) Representative images of protrusion *coiling* on the different fiber diameter categories studied. Left panels show scanning electron microscopic images of base-protrusive fiber combinations.

(D) Temporal evolution of protrusion *coiling* on a 600-nm-diameter fiber.

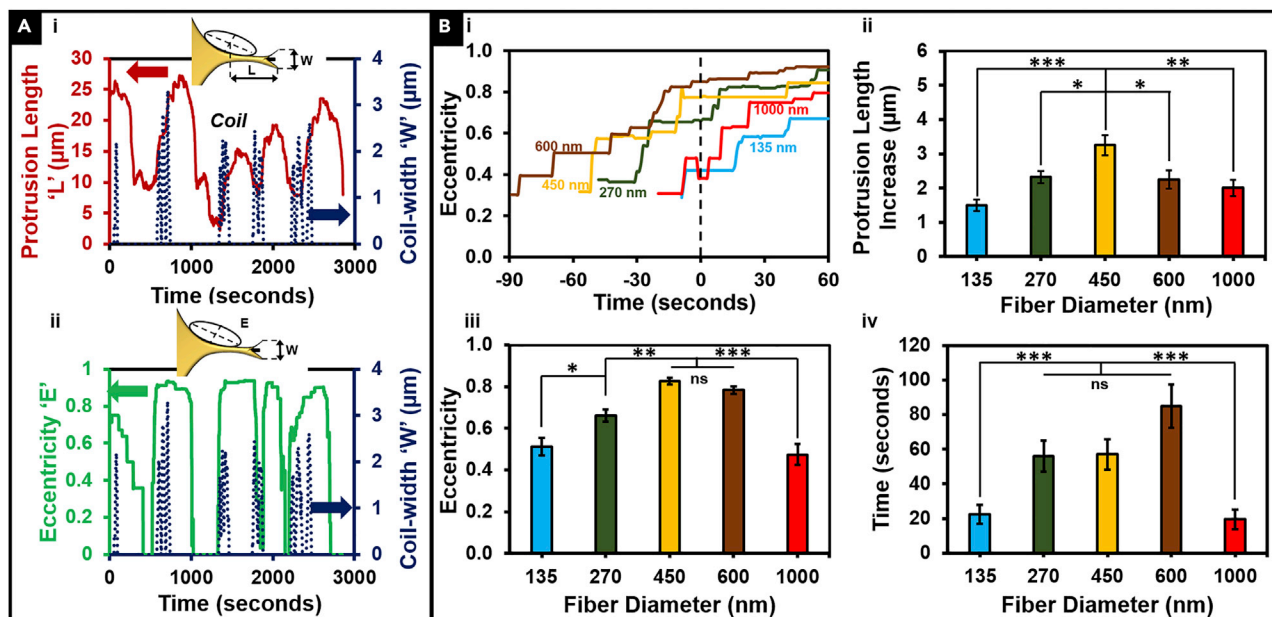
(E) Schematic showing the growth of the protrusion during a *coiling* cycle.

Scale bars, 5 μm. Data are represented as mean ± SEM.

diameter, we found both parameters to increase in a non-linear manner (Figures 3B and 3C), whereas the time taken to reach the maximum *coil* width displayed a biphasic relationship (Figure 3D). Combined with our findings in Figure 2, we conclude that low curvature ~1,000-nm diameter fibers support widest *coils* that initiate independent of protrusion broadening, and do so at the fastest *coil* growth rate.

Granule Translocation Occurs in a Fiber Curvature-Dependent Manner and Coincides with Both the Protrusion Growth and Coiling Cycle

In conjunction with the protrusions *coiling*, we observed that individual granules entered the protrusions at high speeds persistently (Figure 4A). The granule translocation dynamics showed a near-stationary particle



exhibiting fast travel through the protrusion and coming to a near-stationary state again within the protrusion (Video S5). Thus, we inquired if their translocation correlated with the kinetics of coiling.

Near-stationary granules (likely lipid particles, Figure S3) acting as endogenous “tracer particles” were observed to enter the protrusion during the growth phase of the protrusive cycle in $\sim 80\%$ of the cases, with the remaining particles translocating either in a non-growing protrusion or, rarely, in a retracting protrusion (Figure S4). Of the cases of particle translocation during the protrusion growth phase, we found that 69% of them coincided with the coiling cycle (Figure S5). Thus, we inquired if the granule dynamics were being modulated by the fiber curvature. To quantitate the dynamics of granules entering the protrusion, we manually tracked them using ImageJ software to analyze granule speed and persistence (defined as the ratio of the displacement of the granule to the distance covered by the granule during its journey through the protrusion, Figure 4B (i)). We found that for granules entering a protrusion, the speed and persistence both increased with fiber diameter (Figure 4B (ii, iii)). Granule speeds of up to $1.3 \pm 0.2 \mu\text{m/s}$ at high persistence of 0.89 ± 0.03 were achieved for the low-curvature $\sim 1,000$ -nm protrusive fiber diameters representing an ~ 2.3 times increase over the speed ($0.57 \pm 0.06 \mu\text{m/s}$) and a ~ 1.5 times increase over the persistence (0.58 ± 0.03) recorded for the ~ 135 - to 450-nm protrusive fiber diameter cases combined. Interestingly, in cases where multiple granules entered the same protrusion at different times, we observed them to follow a narrow spatial set of paths analogous to highways (Figure S6 shows representative cases on different fiber diameters, and Video S6).

As granules were translocating at high speeds in a persistent fashion into the protrusions, we inquired if the process of translocating could be described by mean square displacement (MSD) method used commonly to describe intracellular granule transport (Caspi et al., 2000; Metzler, 2017). Endogenous granule translocation studied using MSD analysis has been previously shown to range from subdiffusion to superdiffusion regimes indicating random to ballistic transport, respectively (Banks and Fradin, 2005; Bressloff and Newby, 2013; Bronstein et al., 2009; Reverey et al., 2015; Tolić-Nørrelykke et al., 2004; Wachsmuth et al., 2000). The

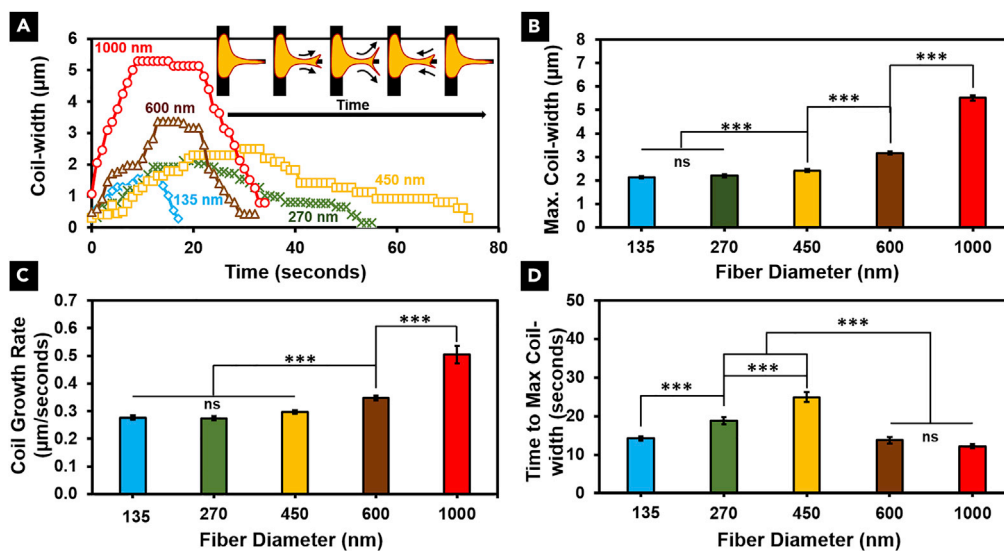


Figure 3. Individual Coiling Dynamics Are Fiber Curvature Dependent

(A) Representative coiling profiles show fiber diameter-dependent dynamics of coiling.

(B and C) (B) Maximum coil width and (C) average coil growth rate increase as a function of protrusive fiber diameter in a non-linear manner.

(D) A biphasic relationship is observed between the time to maximum width and protrusive fiber diameter. In the case of all three parameters (maximum coil width, coil growth rate, and time to maximum width), n values are as follows: 135 nm, 117; 270 nm, 75; 450 nm, 113; 600 nm, 111; 1,000 nm, 77.

See [Methods](#) section for a discussion of the statistical significance parameters. Data are represented as mean \pm SEM. ***p < 0.001.

MSD for random diffusion of a particle through an unobstructed medium in “d” dimensions is given by $\langle R^2 \rangle = 2dDt$ where “R” represents the MSD, “D” is the diffusion coefficient, and “t” is the lag time (Bressloff and Newby, 2013). However, given the densely packed nature of the cell cytoplasm and the presence of molecular motors to assist cargo transport, intracellular transport is better characterized by anomalous diffusion exhibiting a non-linear power-law behavior $\langle R^2 \rangle = 2dDt^\alpha$ where $\alpha = 1$ reverts back to the standard diffusion case (Banks and Fradin, 2005; Saxton, 1994). For $\alpha < 1$, the translocation is termed as subdiffusive, whereas for $\alpha > 1$ the translocation is termed as superdiffusive, and values of $\alpha \sim 2$ represent “ballistic” motion. Our analysis (Figure 4B (iv)) shows that translocation of granules within protrusions occurs in a superdiffusive manner across all the fiber diameter categories studied, and approaches a near-ballistic transport process occurring in protrusions on low-curvature $\sim 1,000$ -nm-diameter fibers.

Finally, given the superdiffusive nature of the granule dynamics, we investigated if molecular motors might play a potential role in the transport of granules in the protrusions. Previously, we have shown that the localization of cytoskeletal components inside individual protrusions is dictated by the protrusion morphology (Koons et al., 2017). Specifically, whereas F-actin and microtubules are present in protrusions of all sizes, the intermediate filament vimentin localized only in mature protrusions (eccentricity ~ 0.8 and higher). Thus, we investigated the effect of pharmacological inhibitors Monastrol (100 μ M) to inhibit kinesin-5 (a microtubule-associated motor protein) and LY249002 (20 μ M) to hinder localization of myosin X (an actin filament-associated motor protein) to the cell leading edge by inhibiting phosphatidylinositol (3,4,5)-trisphosphate (PIP₃) activity (PIP₃ plays a critical role in myosin X recruitment). In both cases (representative cells treated with both drugs shown in Figure S7 and Videos S7, S8, S9, and S10), we observed a change in the protrusive behavior highlighted by an increase in the proportion of relatively short protrusions (<5 μ m in length compared with the average protrusion length of 19 μ m \pm 0.3 μ m; Figure S8). In both cases, washing the drug out recovered the original protrusive behavior. Intriguingly, we found that in both drug cases, there was also a decrease in the proportion of protrusions in which a granule translocation was observed. Analysis of the granule dynamics showed that speed and persistence were unaffected in case of the Monastrol addition, whereas a significant decrease in both speed and persistence was observed with addition of LY249002. Washing out the drugs resulted in recovery of original speed and persistence in both cases

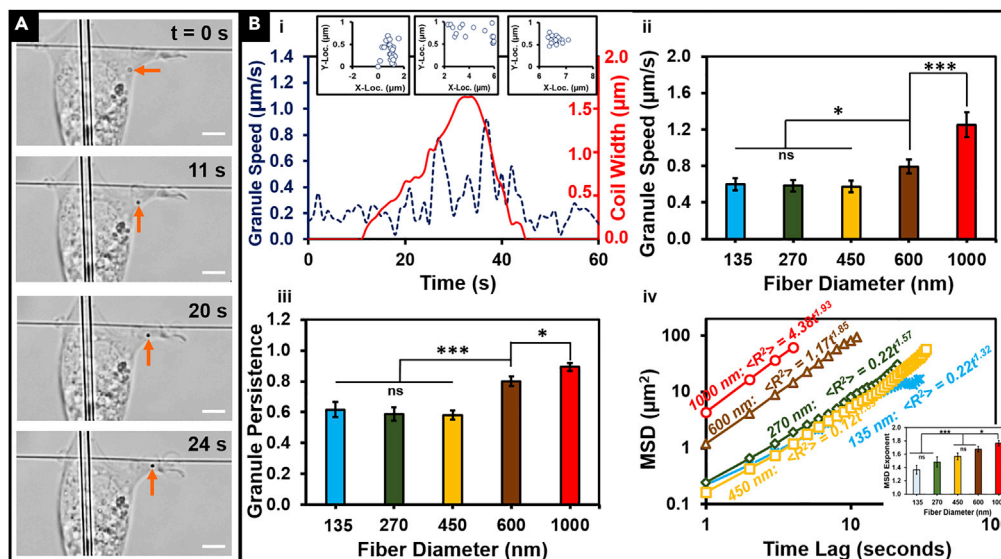


Figure 4. Dynamics of Granules Entering Protrusions

(A) Representative time-lapse images of a single granule (shown by orange arrow) entering a protrusion. Scale bar, 5 μm .

(B) (i) Representative transient profile showing that granule speed (dashed blue line) increases with coil width (solid red line). Inset plots of granule position show near-stationary granules translocate persistently at high speeds during coiling cycle, following which they become near-stationary again. (ii, iii) Speed and persistence of the granules increase with increasing protrusive fiber diameter. (iv) Representative MSD versus time profiles and their calculated MSD for granules on different protrusive fiber diameters show that on all tested diameters, the granules enter the protrusions in a superdiffusive manner (exponent of the scaling law fit >1). Inset, MSD exponent as a function of protrusive fiber diameter shows an increase (on average) with increasing diameter. n values are as follows: 135 nm, 19; 270 nm, 17; 450 nm, 12; 600 nm, 21; 1,000 nm, 20.

See [Methods](#) section for a discussion of the statistical significance parameters. Data are represented as mean \pm SEM. * $p < 0.05$ and *** $p < 0.001$.

([Figure S8](#)). Combined, these results suggest that whereas both kinesin-5 and myosin X motor reduce the instances of granule translocation, myosin X significantly impacts the dynamics of granule translocation.

DISCUSSION

Native fibrous environment surrounding the breast tumor is a complex architecture of fibers with varying diameters, spacing, and orientations ([Figure 5A](#)), which collectively make up pro- and anti-invasive biophysical conditions. Invasion along fibers from the edge of the tumor requires cells to first biophysically sense fibers through formation of rod-like protrusions that can mature into broad structures in a fiber curvature-dependent manner ([Koons et al., 2017](#)). In our study, we quantitate, at single protrusion resolution, the biophysical probing or recognition of curvature of fibers over a wide range of fiber diameters mimicking the surrounding fibrous environment at the tumor periphery (shown by dashed oval in [Figure 5A](#)). We show that fiber curvature modulates the dynamics of the protrusion coiling (size, rate, and time of occurrence). Our findings show that for intermediate-diameter fibers (~ 270 – 600 nm), an increase in eccentricity precedes coiling initiation, whereas for the two ends of the diameter spectrum tested (high curvature, 135 nm, and low curvature, 1,000 nm) coiling occurs independent of protrusion widening (represented by increase in eccentricity, [Figure 2](#)). In contrast, the coil width and its rate of increase positively correlate with the fiber diameter ([Figure 3](#)). The similarities in time taken to reach maximum coil width observed across fibers on either end of tested diameters can be explained by minimal adhesion-driven contractility on high-curvature 135-nm diameter fibers, and conversely low-curvature 1,000-nm-diameter fibers providing adequate surface area for adhesion sites to mature and increase in number. Indeed, supporting this hypothesis are our previous findings that show that cells attached to (1) small 100-nm-diameter nano-scale fibers are unable to spread and remain rounded while actively probing the fiber curvature ([Koons et al., 2017](#)) and (2) large 800-nm-diameter fibers have increased spatial distribution of focal adhesion sites resulting in larger forces ([Sheets et al., 2016](#)). However, the adhesion-based contractility on intermediate

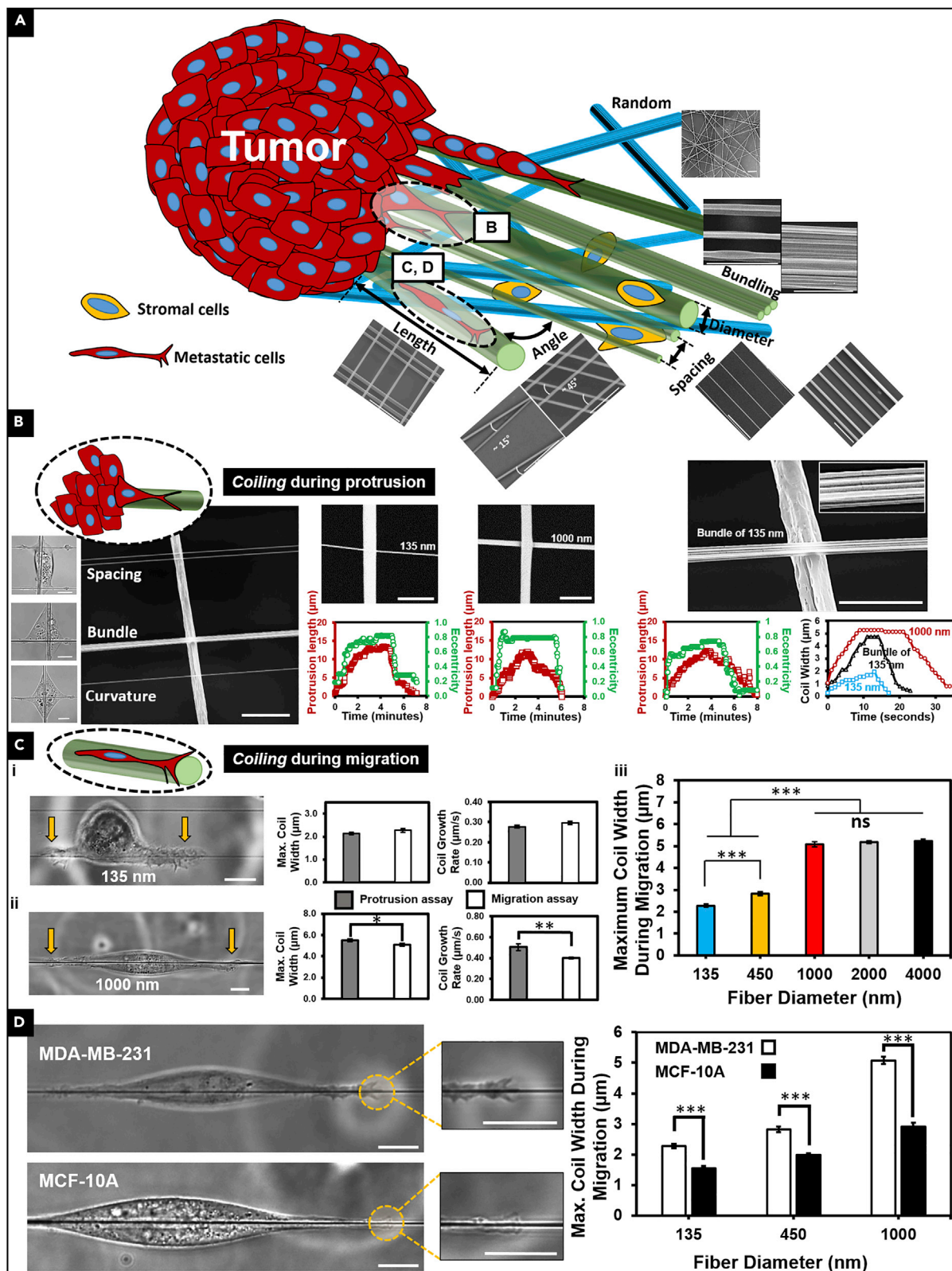


Figure 5. Coiling in Recapitulated *In Vivo* Environments

(A) Schematic showing the heterogeneity observed in environments neighboring breast tumors. Fibers of varied diameters, lengths, orientations, and architectures are interfaced with stromal cells that combined together induce pro- and anti-invasive cell behavior. Inset shows scanning electron microscopic images of fibers deposited in varying configurations (Wang and Nain, 2014) that mimic the native environments including random and aligned configurations. Scale bars, 10 μm .

(B) Cell migration starts with first cells sensing the native environments. Biophysical sensing of fibers can be studied by providing controlled and repeatable fiber architectures (spacing, bundles, and individual fibers of varying curvature). On left are representative phase images of cells on controlled fiber networks (scale bars, 10 μm). Bundling of small-diameter fibers can recover *coil width* kinetics as that of a single large diameter.

(C) *Coiling* during cell migration along fibers. Representative images showing “balled-up” cell morphology during migration on (i) high-curvature 135-nm-diameter fiber and elongated, “spindle” morphology during migration on (ii) low-curvature 1,000-nm diameter fiber. Scale bars, 5 μm . Yellow arrows show simultaneous *coiling* on both sides of the cell. Comparison between *coiling* dynamics on a protrusion assay and migration assay for \sim 135-nm-diameter and \sim 1,000-nm-diameter fiber cases. Sample sizes for the protrusion assay are as follows: 135 nm, 117; 1,000 nm, 77; and for the migration assay are 135 nm, 65; 1,000 nm, 63. (iii) Maximum *coil width* during migration as a function of the fiber diameter. Sample sizes are as follows: 135 nm, 65; 450 nm, 50; 1,000 nm, 63; 2,000 nm, 61; 4,000 nm, 66.

(D) Representative phase images of *coiling* dynamics exhibited by non-tumorigenic MCF-10A and metastatic MDA-MB-231 show diminished *coiling* in non-tumorigenic cell lines. Scale bar, 10 μm . Sample sizes for MDA-MB-231 are as follows: 135 nm, 65; 450 nm, 50; 1,000 nm, 63. Sample sizes for MCF 10A are as follows: 135 nm, 23; 450 nm, 36; 1,000 nm, 20. Data are represented as mean \pm SEM. * $p < 0.05$; ** $p < 0.01$ and *** $p < 0.001$.

fiber diameters remains unclear as the time to reach maximum *coil width* peaks at 450-nm diameter (transient profiles in Figure 3A and data in Figure 3D). Interestingly, substituting single large-diameter fibers with a bundle of smaller diameter fibers recovers *coiling* dynamics on the large-diameter fibers (Figure 5B and Video S11), thus suggesting the role of both mechanical properties and available surface area in biophysical sensing. To determine if *coiling* was also exhibited by other breast cancer cell lines, we repeated the study with highly metastatic ductal carcinoma BT-549 (Figure S9). Our data show similarities in *coiling* dynamics between the two metastatic cancer cell lines.

After extending protrusions to sense the fibrous environment at the tumor interface, breast cancer cells can detach from the primary tumor and begin migrating along linearized collagen fibers toward the circulatory system for subsequent dissemination to secondary sites (Provenzano et al., 2006). Given that protrusion tip *coiling* is observed during protrusion extension, we further enquired if *coiling* also occurred during bulk cell body migration on aligned, single suspended fibers (Figure 5C) of different diameters ranging from \sim 135 nm to \sim 4,000 nm (hereafter referred to as “migration assay”). On the smallest diameter tested (\sim 135 nm), cell spreading was hindered as evidenced by frequent “balling-up” of the cell and blebbing (Video S12). In contrast, on relatively larger diameters (\sim 450 nm and higher, Video S13) tested, cells adopted an elongated “spindle” morphology (Figure 5C (i, ii)). Spindle cells on larger diameter fibers had reduced blebbing, consistent with our previous findings that cell blebbing inversely correlates with cell spread area (Sharma et al., 2013). Interestingly, cells displayed *coiling* at both ends of the cell body (Figure 5C (i, ii) shown by yellow arrows, and Videos S12 and S13), thus suggesting concurrent sensing at opposite poles of rounded and stretched cells. Next, we quantified the dynamics of *coiling* at the tip of cells in line with the direction of migration and compared them with *coiling* quantitated in protrusion assay (perpendicular to the direction of migration) on \sim 135-, \sim 450-, and \sim 1,000-nm diameter fibers. We found that the *coiling* behavior followed the trends obtained using protrusion assay, whereby the width and rate of *coiling* increase in a diameter-dependent manner, and the *coiling cycle* time is the longest for \sim 450-nm-diameter fibers (Figure S10). Notably, we found that on \sim 1,000-nm-diameter fibers that favor cells to form elongated spindle shapes, *coils* were significantly smaller in widths and grew at slower rates compared with the protrusion assay (Figure 5C (i,ii)). Furthermore, the maximum *coil width* in line with migration direction did not change on subsequent larger diameters (\sim 2,000 and \sim 4,000 nm, Figure 5C (iii)). Overall, the similarity in *coiling* on high-curvature fibers (\sim 135 and \sim 450 nm) and differential response on low-curvature fibers (\sim 1,000 nm and above) suggests a possible biophysical adaptation from a sensory to a deterministic migratory response with increase in diameter. How these two responses are utilized by cells to establish adhesion-based contractile machinery in single protrusions or at the two poles of a rounded or stretched cell where *coiling* occurs concurrently remains unclear and is the subject of our future inquiries.

Breast cancer has a well-known predilection for metastasizing to the bone (Lelekakis et al., 1999; Zhou et al., 2016). Following the attachment of previously circulating breast cancer cells to the vascular endothelia of the bone, their subsequent extravasation into the bone marrow compartment is promoted by bone and marrow-derived chemotactic factors (Mastro et al., 2003). On entering the bone marrow, cancer cells encounter a complex array of stromal cells and growth factors embedded in a highly mineralized ECM, which provide a combination of biophysical and biochemical cues that assist in the colonization of the

bone (Gilles et al., 1998; Mastro et al., 2003; Senger and Perruzzi, 1996). The role played by the biochemical cues have been investigated in detail, whereas the influence of the mineralization of the collagen fibers unique to the bone is still unclear. A recent study has shown that MDA-MB-231 breast cancer cells exhibited more rounded morphology on mineralized collagen fibers compared with non-mineralized fibers (Choi et al., 2019). It is unclear if cancer cells could be employing *coiling* as a physical mechanism to aid invasion (easily visualized as a constant drilling process). Thus, we inquired if non-tumorigenic breast cells also displayed *coiling* on fibers of various diameters. Interestingly, we found that non-tumorigenic cancer cells (MCF 10A, [Video S14](#)) exhibit *coiling* less frequently (only ~50% of the cases), and also that the *coil width* was diminished compared with their metastatic counterpart ([Figure 5D](#)). Guided by the *coiling* behavior observed in the breast model, we inquired if *coiling* was observed in other cell types. We find that other cancer models (fibrosarcoma HT1080 and thyroid Hras1) as well as migratory NIH 3T3 fibroblasts ([Videos S15, S16, and S17](#)) to also exhibit *coiling*. Collectively, our data suggest that migratory cells advance on fibers by *coiling*, and the extent of *coiling* is modulated by the fiber curvature. However, how *coiling* is utilized in pro- and anti-migratory environments remains unknown.

In conclusion, using the non-electrospinning STEP platform, we quantitate the biophysical sensing of suspended fibers through *coiling* by cancer cells. We envision that future studies capable of integrating biophysical quantitation presented in this article with membrane tension, curvature-sensing BAR proteins, family of GTPases, and integrin-driven establishment of contractility will link the biophysical *coiling* with biological timing and signaling. In addition, by increasing the complexity of the fibrous environment in a repeatable manner (Sheets et al., 2013), cell morphology-driven *coiling* dynamics could help elucidate the potential role of morphology in cancer cell invasion. Through these future studies, we aim to quantitatively describe the migratory cell decision-making process in pro- and anti-invasive fibrous environments.

Limitations of the Study

We identify key limitations associated with our study along with some of our current and future efforts aimed at addressing them.

At the tumor periphery *in vivo*, tumor cells interact not only with the ECM fibers but also with the neighboring tumor cells with which they can form cell-cell junctions. However, our reductionist approach investigates the *coiling* kinetics of single cells interacting with suspended fibers. Thus, we do not replicate the cell-cell interactions that might potentially have an impact on *coiling* dynamics. In future studies, we aim to include these interactions by interfacing fibers with a monolayer of cells. Using such an approach, we have recently shown protrusion-driven control on invasion modes (single, multichain, and collective) through control of fiber diameter and spacing (Sharma et al., 2017).

The presence of stromal cells provide gradients of soluble biochemical cues in the form of secreted growth factors and chemokines that encourage the invasion of the tumor cells into the surrounding stroma (Oudin and Weaver, 2016). Currently, our studies are conducted in static six-well assays, which do not capture the potential effects of gradients on the *coiling* dynamics. A recent improvement to our method has been integration of fiber networks in custom microfluidic devices (unpublished data). We envision using this assay to calibrate *coiling* dynamics in controlled environments of biophysical and biochemical gradients. Similarly, haptotactic gradients (Rhoads and Guan, 2007) can be set up as we have previously shown that different concentrations of fibronectin cause a differential protrusive response (Koons et al., 2017).

Finally, the ECM surrounding the tumor is composed of a mix of mechanical properties (modulus, bending stiffness, and diameter). We have used fibers made of polystyrene, a commonly used material for culturing cells. The modulus of polystyrene (~1 GPa) matches the modulus of collagen fiber bundles (Silver, 2006; Silver et al., 2003; Wenger et al., 2007), and we have shown the role of bending stiffness (structural stiffness) in modulating cell behavior previously (Meehan and Nain, 2014). Using soft versus stiff polymers (for example, polyurethane with a modulus of ~1–10 MPa) will allow us to understand the role of stiffness in *coiling* kinetics. Furthermore, although we show that a bundle of small-diameter fibers recover *coil widths* of larger diameter fibers, future improvements to fiber spinning with precise control on the number of fibers in a bundle will help in dissecting the role of mechanical properties and curvature in *coiling* kinetics.

METHODS

All methods can be found in the accompanying [Transparent Methods supplemental file](#).

SUPPLEMENTAL INFORMATION

Supplemental Information can be found online at <https://doi.org/10.1016/j.isci.2019.08.023>.

A video abstract is available at <https://doi.org/10.1016/j.isci.2019.08.023#mmc19>.

ACKNOWLEDGMENTS

This work is supported by NSF (1437101 and 1462916) awarded to A.S.N. and NSF CAREER (1454226) to B.B. Authors acknowledge the support from Institute for Critical Technology and Applied Science (ICTAS) and Macromolecules Innovative Institute, Virginia Tech. A.M. and A.S.N. would like to thank members of the STEP Lab, Virginia Tech, for their helpful suggestions and discussions. The authors thank Professor Aime Franco (University of Arkansas) for providing thyroid cancer cells.

AUTHOR CONTRIBUTIONS

Conceptualization, A.S.N.; Methodology, B.B. and A.S.N.; Investigation, A.M., B.B., and A.S.N.; Writing – Original Draft, A.M. and A.S.N.; Writing – Review & Editing, A.M., B.B., and A.S.N.; Funding Acquisition, B.B. and A.S.N.; Resources, B.B. and A.S.N.; Supervision, B.B. and A.S.N.

DECLARATION OF INTERESTS

Fiber networks used in this study were manufactured by STEP fiber manufacturing platform (US Patents 9029149 and 9902932 to A.S.N., and US Patent 9753023 to A.S.N. and B.B.).

Received: December 13, 2018

Revised: April 1, 2019

Accepted: August 13, 2019

Published: September 27, 2019

REFERENCES

- Alblazi, K., and Siar, C. (2015). Cellular protrusions - lamellipodia, filopodia, invadopodia and podosomes - and their roles in progression of orofacial tumours: current understanding. *Asian Pac. J. Cancer Prev.* *16*, 2187–2191.
- Banks, D.S., and Fradin, C. (2005). Anomalous diffusion of proteins due to molecular crowding. *Biophys. J.* *89*, 2960–2971.
- Blanchoin, L., Boujemaa-Paterski, R., Sykes, C., and Plastino, J. (2014). Actin dynamics, architecture, and mechanics in cell motility. *Physiol. Rev.* *94*, 235–263.
- Bressloff, P., and Newby, J. (2013). Stochastic models of intracellular transport. *Rev. Mod. Phys.* *85*, 136–191.
- Bronstein, I., Israel, Y., Kepten, E., Mai, S., Shav-Tal, Y., Barkai, E., and Garini, Y. (2009). Transient anomalous diffusion of telomeres in the nucleus of mammalian cells. *Phys. Rev. Lett.* *103*, 018102.
- Buccione, R., Orth, J.D., and McNiven, M.A. (2004). Foot and mouth: podosomes, invadopodia and circular dorsal ruffles. *Nat. Rev.* *5*, 647–657.
- Carey, S.P., Goldblatt, Z.E., Martin, K.E., Romero, B., Williams, R.M., and Reinhart-King, C.A. (2016). Local extracellular matrix alignment directs cellular protrusion dynamics and migration through Rac1 and FAK local extracellular matrix alignment directs cellular protrusion dynamics and migration through Rac1 and FAK. *Integr. Biol. Integr. Biol.* *8*, 821–835.
- Caspi, A., Granek, R., and Elbaum, M. (2000). Enhanced diffusion in active intracellular transport. *Phys. Rev. Lett.* *85*, 5655–5658.
- Choi, S., Friedrichs, J., Song, Y.H., Werner, C., Estroff, L.A., and Fischbach, C. (2019). Intrafibrillar, bone-mimetic collagen mineralization regulates breast cancer cell adhesion and migration. *Biomaterials* *198*, 95–106.
- Clainche, C.L.E., and Carlier, M. (2008). Regulation of actin assembly associated with protrusion and adhesion in cell migration. *Physiol. Rev.* *88*, 489–513.
- Clark, R.A.F., Lanigan, J.M., DellaPelle, P., Manseau, E., Dvorak, H.F., and Colvin, R.B. (1982). Fibronectin and fibrin provide a provisional matrix for epidermal cell migration during wound reepithelialization. *J. Invest. Dermatol.* *79*, 264–269.
- Fraleigh, S.I., Wu, P., He, L., Feng, Y., Krisnamurthy, R., Longmore, G.D., and Wirtz, D. (2015). Three-dimensional matrix fiber alignment modulates cell migration and MT1-MMP utility by spatially and temporally directing protrusions. *Sci. Rep.* *5*, 14580.
- Friedl, P., and Wolf, K. (2010). Plasticity of cell migration: a multiscale tuning model. *J. Cell Biol.* *188*, 11–19.
- Gilles, C., Bassuk, J.A., Pulyaeva, H., Sage, E.H., Foidart, J.M., and Thompson, E.W. (1998). SPARC/osteonection induces matrix metalloproteinase 2 activation in human breast cancer cell lines. *Cancer Res.* *58*, 5529–5536.
- Harland, B., Walcott, S., and Sun, S.X. (2011). Adhesion dynamics and durotaxis in migrating cells. *Phys. Biol.* *8*, 015011.
- Kennedy, K.M., Bhaw-Luximon, A., and Jhurry, D. (2017). Cell-matrix mechanical interaction in electrospun polymeric scaffolds for tissue engineering: implications for scaffold design and performance. *Acta Biomater.* *50*, 41–55.
- Koons, B., Sharma, P., Ye, Z., Mukherjee, A., Lee, M.H., Wirtz, D., Behkam, B., and Nain, A.S. (2017). Cancer protrusions on a tightrope: nanofiber curvature contrast quantitates single protrusion dynamics. *ACS Nano* *11*, 12037–12048.
- Lelekakis, M., Moseley, J.M., Martin, T.J., Hards, D., Williams, E., Ho, P., Lowen, D., Javni, J., Miller, F.R., Slavin, J., and Anderson, R.L. (1999). A novel orthotopic model of breast cancer metastasis to bone. *Clin. Exp. Metastasis* *17*, 163–170.
- Linder, S. (2007). The matrix corroded: podosomes and invadopodia in extracellular matrix degradation. *Trends Cell Biol.* *17*, 107–117.
- Lo, C.M., Wang, H.B., Dembo, M., and Wang, Y.L. (2000). Cell movement is guided by the rigidity of the substrate. *Biophys. J.* *79*, 144–152.
- Machacek, M., Hodgson, L., Welch, C., Elliott, H., Pertz, O., Nalbant, P., Abell, A., Johnson, G.L., Hahn, K.M., and Danuser, G. (2009). Coordination of Rho GTPase activities during cell protrusion. *Nature* *461*, 99–103.

- Mastro, A.M., Gay, C.V., and Welch, D.R. (2003). The skeleton as a unique environment for breast cancer cells. *Clin. Exp. Metastasis* 20, 275–284.
- Meehan, S., and Nain, A.S. (2014). Role of suspended fiber structural stiffness and curvature on single-cell migration, nucleus shape, and focal-adhesion-cluster length. *Biophys. J.* 107, 2604–2611.
- Meshel, A.S., Wei, Q., Adelstein, R.S., and Sheetz, M.P. (2005). Basic mechanism of three-dimensional collagen fibre transport by fibroblasts. *Nat. Cell Biol.* 7, 157–164.
- Metzler, R. (2017). Anomalous diffusion in membranes and the cytoplasm of biological cells. *Biophys. J.* 112, 476a.
- Nain, A.S., Sitti, M., Jacobson, A., Kowalewski, T., and Amon, C. (2009). Dry spinning based Spinneret based tunable engineered parameters (STEP) technique for controlled and aligned deposition of polymeric nanofibers. *Macromol. Rapid Commun.* 30, 1406–1412.
- Nain, A.S., and Wang, J. (2013). Polymeric nanofibers: isodiametric design space and methodology for depositing aligned nanofiber arrays in single and multiple layers. *Polym. J.* 45. <https://doi.org/10.1038/pj.2013.1>.
- Oudin, M.J., and Weaver, V.M. (2016). Physical and chemical gradients in the tumor microenvironment regulate tumor cell invasion, migration, and metastasis. *Cold Spring Harb. Symp. Quant. Biol.* 81, 189–205.
- Pollard, T.D., and Borisy, G.G. (2003). Cellular motility driven by assembly and disassembly of actin filaments. *Cell* 112, 453–465.
- Ponti, A., Machacek, M., Gupton, S.L., Waterman-Storer, C.M., and Danuser, G. (2004). Two distinct actin networks drive the protrusion of migrating cells. *Science* 305, 1782–1786.
- Provenzano, P.P., Eliceiri, K.W., Campbell, J.M., Inman, D.R., White, J.G., and Keely, P.J. (2006). Collagen reorganization at the tumor-stromal interface facilitates local invasion. *BMC Med.* 4, 38.
- Reverey, J.F., Jeon, J.-H., Bao, H., Leippe, M., Metzler, R., and Selhuber-Unkel, C. (2015). Superdiffusion dominates intracellular particle motion in the supercrowded cytoplasm of pathogenic *Acanthamoeba castellanii*. *Sci. Rep.* 5, 11690.
- Rhoads, D.S., and Guan, J.-L. (2007). Analysis of directional cell migration on defined FN gradients: role of intracellular signaling molecules. *Exp. Cell Res.* 313, 3859–3867.
- Riching, K.M., Cox, B.L., Salick, M.R., Pehlke, C., Riching, A.S., Ponik, S.M., Bass, B.R., Crone, W.C., Jiang, Y., Weaver, A.M., et al. (2014). 3D collagen alignment limits protrusions to enhance breast cancer cell persistence. *Biophys. J.* 107, 2546–2558.
- Saxton, M.J. (1994). Anomalous diffusion due to obstacles: a Monte Carlo study. *Biophys. J.* 66, 394–401.
- Senger, D.R., and Perruzzi, C.A. (1996). Cell migration promoted by a potent GRGDS-containing thrombin-cleavage fragment of osteopontin. *Biochim. Biophys. Acta* 1314, 13–24.
- Sharma, P., Ng, C., Jana, A., Padhi, A., Szymanski, P., Lee, J.S.H., Behkam, B., and Nain, A.S. (2017). Aligned fibers direct collective cell migration to engineer closing and nonclosing wound gaps. *Mol. Biol. Cell* 28, 2579–2588.
- Sharma, P., Sheets, K., Elankumaran, S., and Singh Nain, A. (2013). The mechanistic influence of aligned nanofibers on cell shape, migration and blebbing dynamics of glioma cells. *Integr. Biol. Integr. Biol.* 5, 1036–1044.
- Sheets, K., Wang, J., Zhao, W., Kapania, R., and Nain, A.S. (2016). Nanonet force microscopy for measuring cell forces. *Biophys. J.* 111, 197–207.
- Sheets, K., Wunsch, S., Ng, C., and Nain, A.S. (2013). Shape-dependent cell migration and focal adhesion organization on suspended and aligned nanofiber scaffolds. *Acta Biomater.* 9, 7169–7177.
- Silver, F.H. (2006). *Mechanosensing and Mechanochemical Transduction in Extracellular Matrix: Biological, Chemical, Engineering, and Physiological Aspects* (Springer Science & Business Media).
- Silver, F.H., Freeman, J.W., and Sehra, G.P. (2003). Collagen self-assembly and the development of tendon mechanical properties. *J. Biomech.* 36, 1529–1553.
- Starke, J., Maaser, K., Wehrle-Haller, B., and Friedl, P. (2013). Mechanotransduction of mesenchymal melanoma cell invasion into 3D collagen lattices: filopod-mediated extension-relaxation cycles and force anisotropy. *Exp. Cell Res.* 319, 2424–2433.
- Tolić-Nørrellykke, I.M., Munteanu, E.-L., Thon, G., Oddershede, L., and Berg-Sørensen, K. (2004). Anomalous diffusion in living yeast cells. *Phys. Rev. Lett.* 93, 078102.
- Ushiki, T. (2002). Collagen fibers, reticular fibers and elastic fibers. A comprehensive understanding from a morphological viewpoint. *Arch. Histol. Cytol.* 65, 109–126.
- Wachsmuth, M., Waldeck, W., and Langowski, J. (2000). Anomalous diffusion of fluorescent probes inside living cell nuclei investigated by spatially-resolved fluorescence correlation spectroscopy. *J. Mol. Biol.* 298, 677–689.
- Wang, J., and Nain, A.S. (2014). Suspended micro/nanofiber hierarchical biological scaffolds fabricated using non-electrospinning STEP technique. *Langmuir* 30, 13641–13649.
- Weaver, A.M. (2006). Invadopodia: specialized cell structures for cancer invasion. *Clin. Exp. Metastasis* 23, 97–105.
- Weber, M., Hauschild, R., Schwarz, J., Moussion, C., de Vries, I., Legler, D.F., Luther, S.A., Bollenbach, T., and Sixt, M. (2013). Interstitial dendritic cell guidance by haptotactic chemokine gradients. *Science* 339, 328–332.
- Wenger, M.P.E., Bozec, L., Horton, M.A., and Mesquida, P. (2007). Mechanical properties of collagen fibrils. *Biophys. J.* 93, 1255–1263.
- Wolf, K., and Friedl, P. (2009). Mapping proteolytic cancer cell-extracellular matrix interfaces. *Clin. Exp. Metastasis* 26, 289–298.
- Wu, C., Asokan, S.B., Berginski, M.E., Haynes, E.M., Sharpless, N.E., Griffith, J.D., Gomez, S.M., and Bear, J.E. (2012). Arp2/3 is critical for lamellipodia and response to extracellular matrix cues but is dispensable for chemotaxis. *Cell* 148, 973–987.
- Zhou, X., Zhu, W., Nowicki, M., Miao, S., Cui, H., Holmes, B., Glazer, R.I., and Zhang, L.G. (2016). 3D bioprinting a cell-laden bone matrix for breast cancer metastasis study. *ACS Appl. Mater. Interfaces* 8, 30017–30026.
- Zigmond, S.H., Foxman, E.F., and Segall, J.E. (2001). Chemotaxis assays for eukaryotic cells. *Curr. Protoc. Cell Biol.*, Chapter 12, Unit 12.1. <https://doi.org/10.1002/0471143030.cb1201s00>.

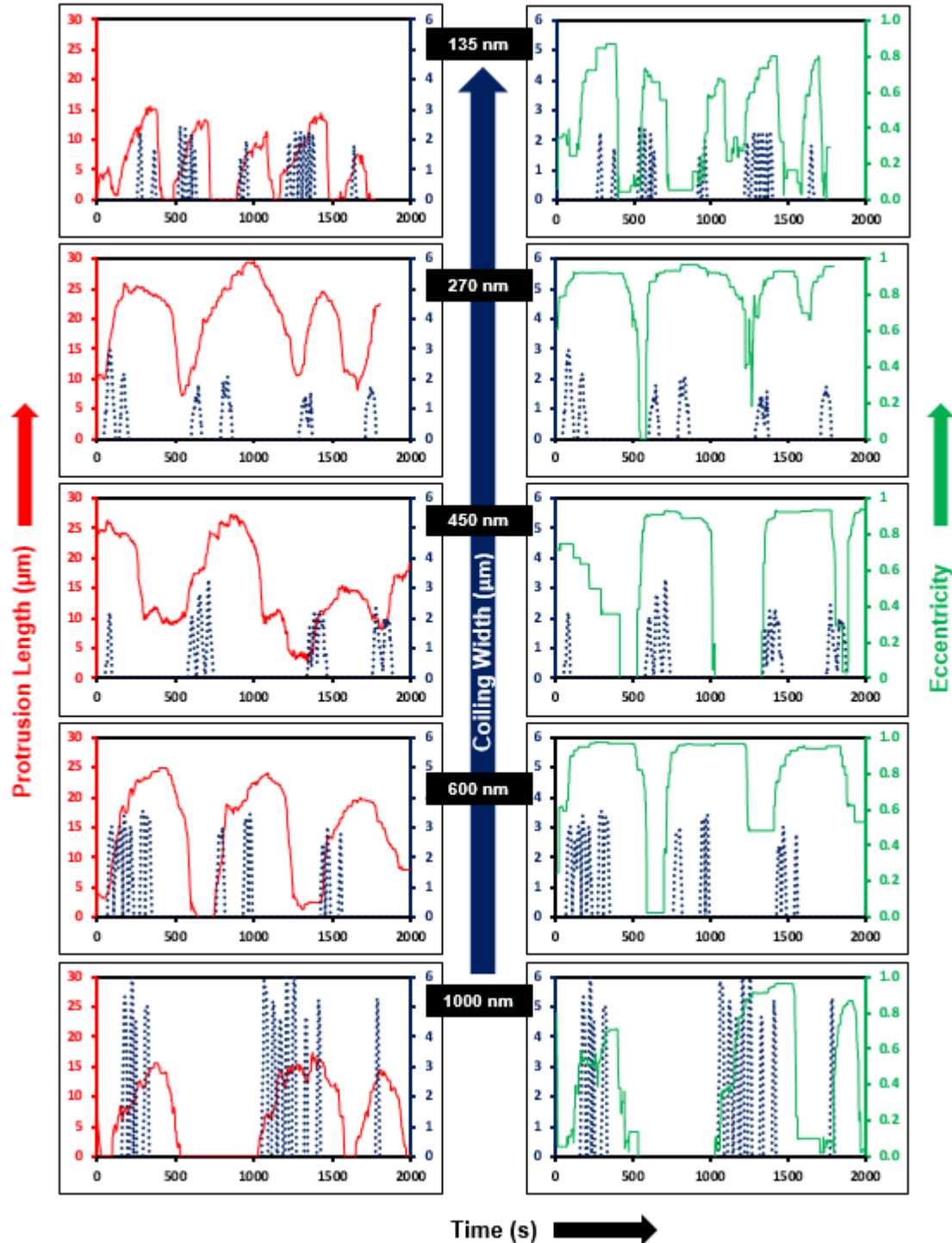
ISCI, Volume 19

Supplemental Information

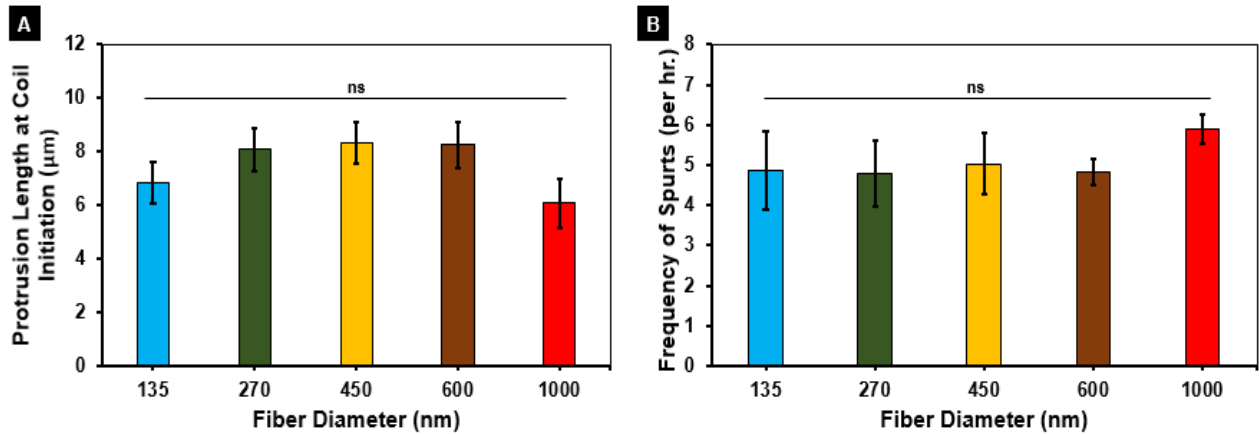
**Cancer Cells Sense Fibers by *Coiling*
on them in a Curvature-Dependent Manner**

Apratim Mukherjee, Bahareh Behkam, and Amrinder S. Nain

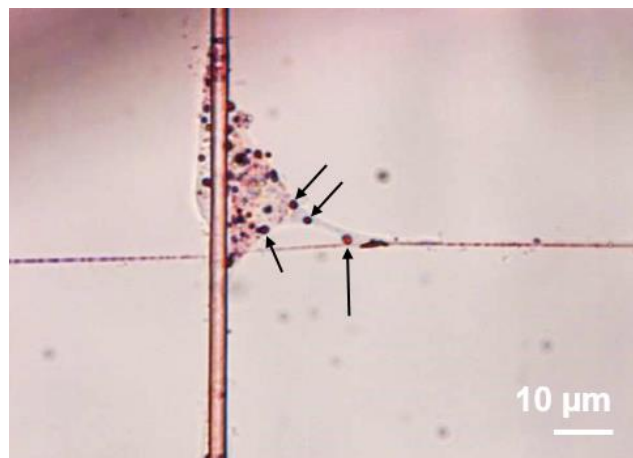
Supplemental Figures



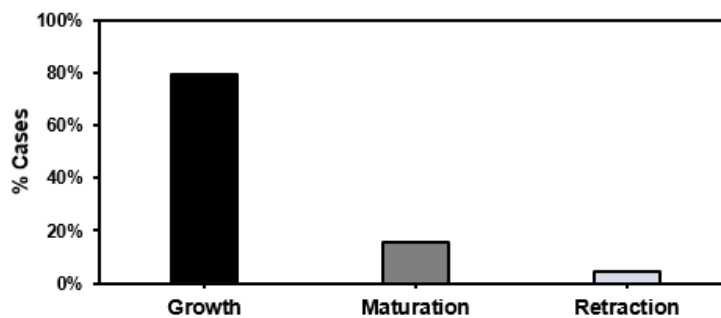
Supplemental Figure S1. Representative protrusive profiles for the different *protrusive fiber* diameters studied, related to Figure 2. The mechanism of *coiling* behavior occurring in spurts during the protrusion growth is conserved across fiber diameters. Each row of plots is for the same fiber diameter.



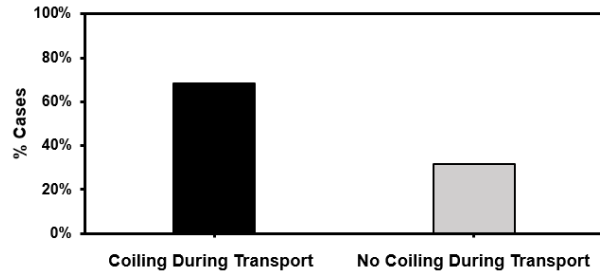
Supplemental Figure S2: Average protrusion length at the initiation of coiling and subsequent *coiling* frequency as a function of fiber diameter, related to Figure 2. Both the (A) average protrusion length at the onset of *coiling* and (B) frequency of *coiling* spurts are independent of fiber diameter. n values for (A) are as follows: 135 nm – 20, 270 nm – 21, 450 nm – 23, 600 nm – 20, 1000 nm – 20. n values for (B) are 10 for each fiber diameter. See Methods section for a discussion of the statistical significance parameters.



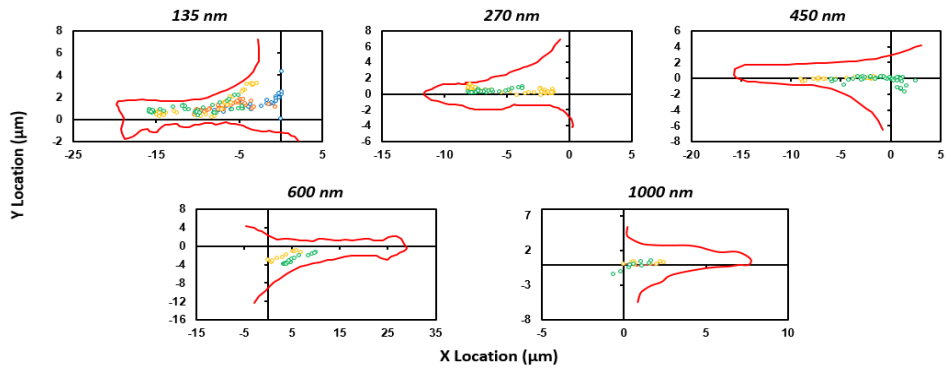
Supplemental Figure S3: Oil Red O staining image, related to Figure 4. Representative cell after Oil Red O staining showing the granules in dark red (selective granules inside a protrusion indicated by black arrows).



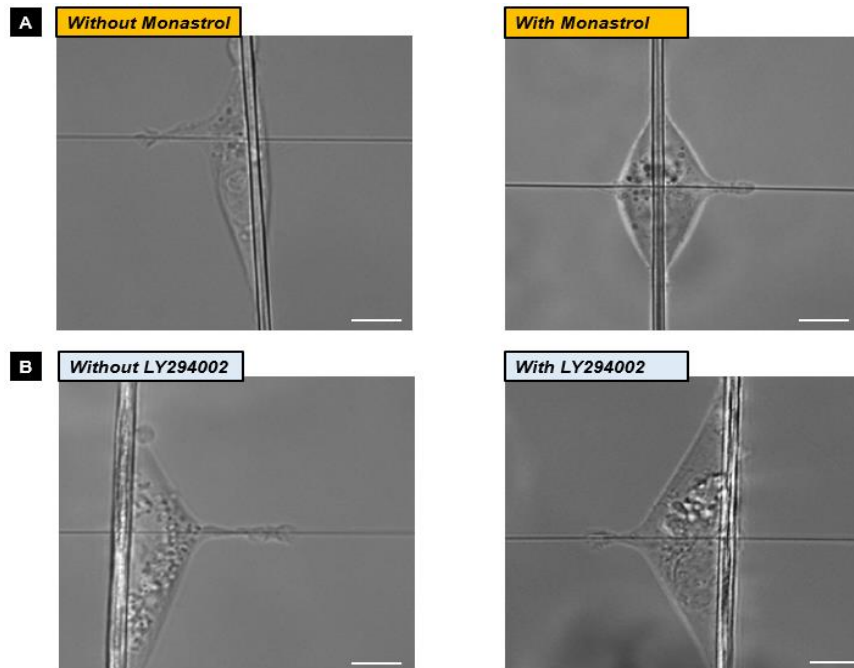
Supplemental Figure S4: Linking granule transport to the protrusive cycle, related to Figure 4. % of total granule transport cases which occurred during the different stages of the *protrusive cycle*. n = 89 granules.



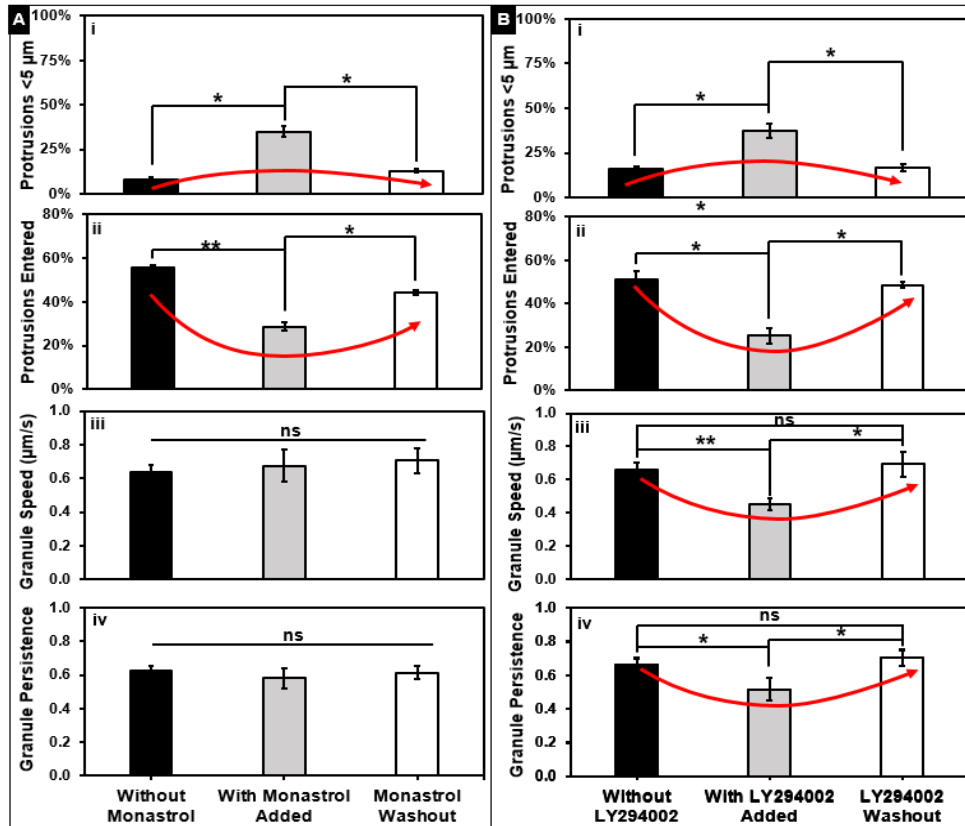
Supplemental Figure S5: Linking granule transport to the *coiling* cycle, related to Figure 4. Percentage of total granule transport cases during protrusion growth which coincide with tip *coiling*. n = 71 granules.



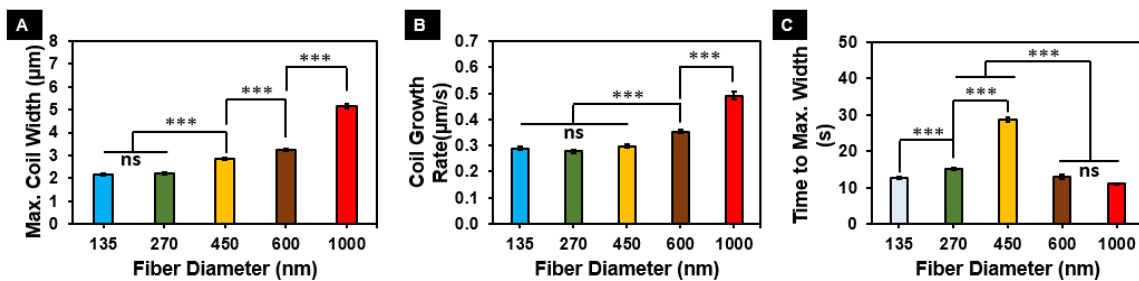
Supplemental Figure S6: Representative profiles showing that granules enter protrusions along a tightly defined set of routes, related to Figure 4. Representative protrusion profiles (in red) and granule trajectories (circles) for the different fiber diameters are shown.



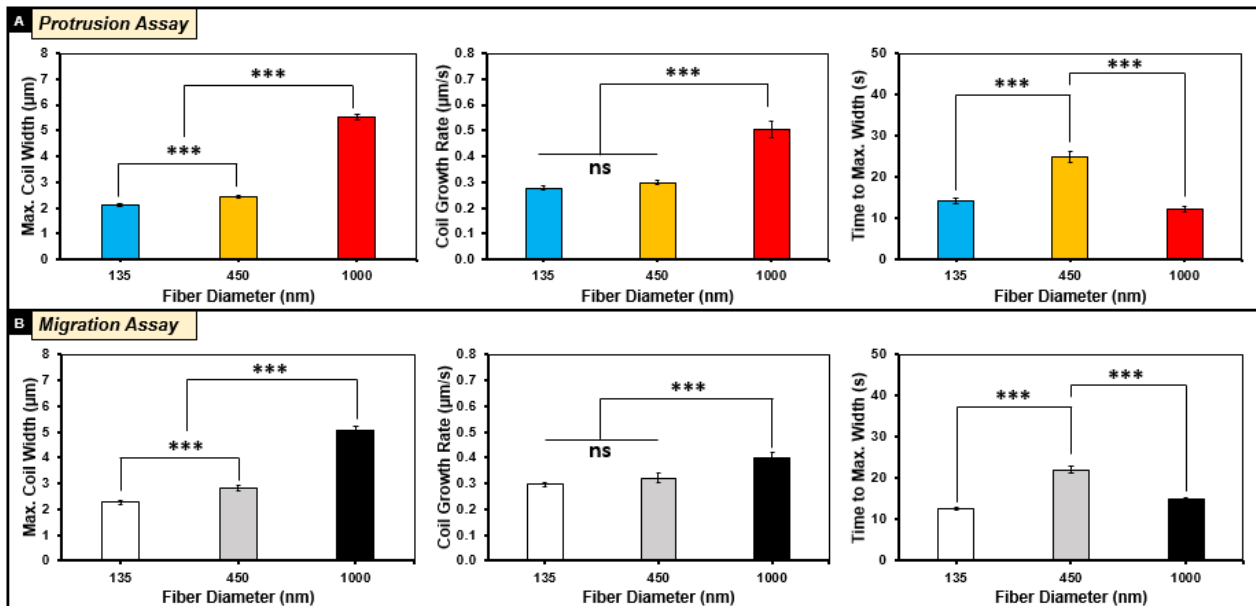
Supplemental Figure S7: Representative images of MDA-MB-231 cells before and after drug treatment, related to Figure 4. (A) Treatment with 100 μm Monastrol and (B) Treatment with 20 μm LY294002.



Supplemental Figure S8: Pharmacological inhibition of cytoskeletal motors, related to Figure 4. Here panel (A) represents the results using Monastrol while panel (B) represents the results using LY294002. In both cases, we recorded (i) the percentage of protrusions lower than 5 μm in length, (ii) the percentage of protrusions in which granule translocation was observed, (iii) granule speed and (iv) granule persistence for the control case (without drugs added), with the drug added and finally, after drug washout. *n* values for the Monastrol study are as follows: 64, 43, and 70 protrusions recorded for the cases without Monastrol, with Monastrol and Monastrol washout cases respectively. 33, 8, and 27 granule translocation cases observed in the without Monastrol, with Monastrol and washout cases respectively. *n* values for the LY294002 study are as follows: 55, 60, and 52 protrusions recorded for the cases without LY294002, with LY294002 and washout respectively. 24, 9 and 21 granule translocation cases observed in experiments without LY294002, with LY294002 and washout cases respectively. For the % protrusions entered, only the protrusions $>5 \mu\text{m}$ were considered. See Methods section for a discussion of the statistical significance parameters.



Supplemental Figure S9: Quantifying coiling dynamics for BT-549 cells, related to Figure 3. (A) Maximum coil width, (B) Coil growth rate and (C) Time to maximum coil width as a function of fiber diameter. *n* values are as follows: 135 nm – 65, 270 nm – 63, 450 nm – 61, 600 nm – 61, 1000 nm – 60.



Supplemental Figure S10: *Coiling* dynamics on both protrusion and migration assays exhibit the same trend, related to Figure 5. Quantification of *coiling* dynamics for MDA-MB-231 cells on (A) protrusion assay and (B) migration assay as a function of fiber diameter. n values for the protrusion assay are: ~135 nm – 117, ~450 nm – 113, and ~1000 nm – 77. n values for the migration assay are: ~135 nm – 65, ~450 nm – 50, and ~1000 nm – 63.

Transparent Methods:

Non-electrospinning STEP Protrusion Platform: The previously reported STEP method(Nain et al., 2009) was used to spin a crosshatch network of large diameter, “strut-like” base fibers orthogonal to which were deposited the smaller diameter *protrusive* fibers. The networks were then fused at fiber intersections. The base fibers were fabricated to be at least 2 μm whereas 5 different *protrusive fiber* diameters were used: ~ 135 nm, ~ 270 nm, ~ 450 nm, ~ 600 nm, and ~ 1000 nm. Polystyrene (PS, Scientific Polymer Products, Ontario, NY, MW = 2×10^6 g mol⁻¹) of $\sim 2 \times 10^6$ g/mol molecular weight was dissolved in *p-xylene* (Fischer Scientific, Pittsburgh, PA) at 7, 8, 10, 12 and 14% (w/w) to prepare the polymer solutions prior to spinning the ~ 135 nm, ~ 270 nm, ~ 450 nm, ~ 600 nm and ~ 1000 nm diameter fibers respectively. To prepare the ~ 2000 nm diameter *base fibers*, polystyrene of $\sim 2 \times 10^6$ g/mol molecular weight was dissolved in a 1:1 xylene:dimethylformamide solution at a 10% (w/w) concentration. To prepare the ~ 4000 nm diameter fibers for the migration assay, polystyrene of $\sim 15 \times 10^6$ g/mol molecular weight was dissolved in p-xylene at a 6% (w/w) concentration. The interfiber spacing was tuned to be ~ 200 μm between the *base fibers* and ~ 75 μm between the *protrusive fibers*.

Cell culture, Seeding: MDA-MB-231 mammary ductal adenocarcinoma cells were cultured in Leibovitz’s L-15 media (Thermo Fisher Scientific, Waltham, MA) supplemented with 10% Fetal Bovine Serum (Thermo Fisher Scientific, Waltham, MA). The culture was maintained in an incubator without CO₂ at 37 °C. BT-549 mammary ductal carcinoma cells were cultured in RPMI media (Thermo Fisher Scientific, Waltham, MA) supplemented with 10% Fetal Bovine Serum. MCF 10A non-tumorigenic breast epithelial cells were cultured using the MEGM growth kit (Lonza, Walkersville, MD). HT1080 fibrosarcoma cells were cultured in DMEM media (Thermo Fisher Scientific, Waltham, MA) supplemented with 10% Fetal Bovine Serum. Hras1 thyroid cancer cells were obtained from an Hras^{G12V}/Pten KO murine thyroid tumor(Jolly et al., 2016) and were cultured in F12 media (Thermo Fisher Scientific, Waltham, MA) supplemented with 10% Fetal Bovine Serum. NIH/3T3 fibroblasts were cultured in DMEM (Thermo Fisher Scientific, Waltham, MA) supplemented with 10% Fetal Calf Serum (ATCC, Manassas, VA). The BT-549, MCF 10A, HT1080, Hras1 and NIH 3T3 cultures were maintained in an incubator with CO₂ at 37 °C. To prepare for imaging the scaffolds were first glued down to the glass bottom of 6-well dishes (MatTek Corp., Ashland, MA) using

sterile high-vacuum grease (Dow Corning, Midland, MI). The scaffolds were sterilized using a 70% ethanol wash followed by two PBS rinses (Thermo Fisher Scientific). Subsequently, the fibers were coated with 4 $\mu\text{g/ml}$ Fibronectin (Invitrogen, Carlsbad, CA) for ~ 2 hours prior to cell seeding. At $\sim 80\%$ confluence, the cell culture was trypsinized using 0.25% Trypsin-EDTA (ATCC, Manassas, VA) and the cells were then re-suspended and diluted in culture medium. Cells were seeded with a density of $\sim 300,000$ cells/ml on the scaffolds and were allowed to attach to the fibers for ~ 3 hours. Finally, once cell attachment to the fibers was confirmed, each well was filled with 3 ml of media.

Oil Red O Staining: In order to prepare for Oil Red O staining, the cells on the protrusion assay were fixed in 4% paraformaldehyde for 15 minutes followed by two PBS rinses. 0.5% Oil Red O (Sigma Aldrich, St. Louis, MO) solution was prepared in $\geq 99.9\%$ isopropanol. A working solution was prepared by diluting the Oil Red O solution in DI water in a 3:2 ratio. Before using the working solution, it was passed through a 0.2 μm syringe filter. 3 ml of the working solution was then added to each well of the fixed cells and kept in the wells for 15 minutes. Subsequently, the working solution was washed off by four DI water rinses.

Pharmacological Inhibitors: In order to inhibit kinesin-5 activity, 100 μm Monastrol (Millipore Sigma, St. Louis, Missouri) was used with an incubation period of 3 hours. In order to impair myosin X localization by inhibiting PIP_3 activity, 20 μm LY294002 (Millipore Sigma, St. Louis, Missouri) was used with an incubation period of 3 hours. In both cases, washout was performed by aspirating the media and washing the wells twice with PBS followed by addition of regular media. To determine the effect of the drug additions on granule dynamics, we quantified the percentage of total protrusions extended in which a granule was observed to translocate in addition to quantifying the granule speed and persistence.

Microscopy and Imaging: The cells were imaged using the AxioObserver Z.1 (with mRm camera) microscope (Carl Zeiss, Germany) at 63x (water based immersion) magnification with 1 second time imaging interval. Care was taken to ensure that only cells which were not interacting with other cells were imaged. The obtained videos were analyzed using ImageJ (National Institutes of Health, Bethesda, MD). Granules were tracked manually using ImageJ.

Statistical Analysis: Statistical analysis of the data was performed using RStudio (RStudio, Boston, MA) software. Shapiro-Wilks normality test was performed to test for the normality of the data. Analysis of

variance (ANOVA) test was used to test for statistical significance between different data sets. The following symbols are used throughout the paper to represent significance levels: * <math><0.05</math>, ** <math><0.01</math>, and *** <math><0.001</math>. If there is no comparison shown between any data sets it implies that they are not significant. All error bars represent standard error of mean.